Nanoscale

PAPER

View Article Online
View Journal | View Issue

Cite this: *Nanoscale*, 2025, **17**, 1053

Particle surface engineering at the nano-micro scale interfaces of metal-nonmetal bonded polymeric coatings: experimental and *in silico* evaluations

Suman Yadav,[a] Sarvesh Kumar Pandey*[b] and Shikha Awasthi *[a]

Polyvinyl alcohol (PVA) is a well-known and cost-effective synthetic polymer that offers a variety of applications, including medical, food, aerospace, automotive, and material industries, for the construction of structures. However, the weak adhesion, low wear resistance, and mechanical properties of PVA usually limit their functionality and durability. Herein, the strength and bonding of the polymeric matrix were enhanced by metallization and reinforcement of carbonaceous allotropes. The nickel and diamond-containing PVA coating (PVA-Ni-D) was found to be the most wear-resistant coating with the lowest wear rate (7.34×10^{-3} mm^3), reduced penetration depth (19.2 μm) and highest scratch hardness (4.92 GPa) compared to the carbon nanotubes (PVA-Ni-CNT) and graphene (PVA-Ni-Gr)-containing composite coatings. The significant enhancement in the wear resistance of the composite coatings was further linked with the contact depth, contact radius and shear stress, as calculated by different theoretical models. The results from the interfacial interaction estimation demonstrated a strong strengthening of the diamond particles with the matrix due to particle-matrix interaction. Meanwhile, the large surface area per unit volume (in the case of CNT and graphene) results in inter-particle interactions, followed by easy sliding of these reinforcements from the matrix, which causes decreased mechanical strength and tribological performance. Density functional theory (DFT) was used to perform electronic structure calculations on the metallized polymeric composite models (two configurations were used), and the *in silico* research seemed to promote relevant and evocative outputs for the diamond-encapsulated PVA-Ni system. Therefore, the improved strength and bonding of the PVA-Ni-D coating make it a promising composite coating for multi-functional applications in materials industries.

Received 21st August 2024,
Accepted 8th November 2024

DOI: 10.1039/d4nr03431g

rsc.li/nanoscale

1. Introduction

Polyvinyl alcohol (PVA) is a synthetic (thermoplastic) polymer that has a wide variety of applications mainly in film coatings and is well characterized in terms of its toxicity and biocompatibility in the medical, textile, food, and material industries. PVA is cheap, has excellent interfacial adhesion properties with reinforcement materials, and possesses excellent thermal properties that are useful for composite fabrication.[1] In the last fifty years, nearly every industry in the world, including manufacturing, transportation, building, mining, and education, has adopted and profited from the use of polymer-based materials. The use of polymers has increased owing to their cost-effectiveness and unique characteristics. Because of their low weight, low cost, and processing benefits, polymers and their composites are widely employed in the aerospace, automotive, electronic, and sports industries for the construction of structures. However, intrinsic flaws, including low bioactivity, low adhesion, weak wear resistance, and low thermal and electrical conductivity, in the polymeric materials' surfaces usually limit their functionality and longevity.[2] The polymer coatings' efficacy and lifespan are improved by the incorporation of metals and metal oxide. According to C. Verma *et al.*,[3] the metal–polymer and metal oxide polymer frameworks have anti-corrosion properties, providing excellent surface protection. This facilitates their use in many applications in various industries, including materials and coating, supercapacitors, catalysis, automotive, and ships.[3]

The automobile and aerospace sectors are the main users of nickel, with applications including wheels, pinion shafts, slip yokes, carburettors, gasoline connectors, supercapacitors, power generation turbines, rocket engines, magnetic and electrical devices, and metal manufacturing.[4] Practically speaking,

[a]*Department of Chemistry, Manipal University Jaipur, Jaipur–303007, Rajasthan, India. E-mail: shikha.awasthi@jaipur.manipal.edu*
[b]*Department of Chemistry, Maulana Azad National Institute of Technology Bhopal, Bhopal–462 003, Madhya Pradesh, India. E-mail: sarvesh@manit.ac.in*

nickel plating can provide a surface with greater thickness, enhanced wear resistance, good thermal stability, a high surface-volume- ratio and corrosion resistance. It can enhance the attractiveness, lustre, and brightness.[5,6] Nickel is frequently employed because it also offers superior adhesive capabilities for subsequent coating layers. It protects lightweight plastics from abrasion and offers superior protection against electromagnetic interference (EMI).[7,8] Nickel-based coatings are often used in aerospace applications, defence, automotive, and electronics.[9,10] Because of their facile modification, conductivity, surface area, hardness, electrical properties, thermal stability, high corrosion resistance, and biocompatibility, carbonaceous allotropes (CNT, graphene, diamond) are beneficial and have a larger range of applications as electrodes, supercapacitors, sensors, and electrodes.[11,12]

PVA has high water solubility and absorption capacity, which is a drawback of the PVA films, so its fabrication with carbonaceous reinforcement increases the mechanical strength of the PVA composite. Enhanced hardness and coefficient of friction (COF) and less water uptake were observed by Sonker *et al.*[13] in a PVA cross-linked composite reinforced with tungsten disulfide nanotube nanoparticles. An enhancement in the corrosion resistance, adhesion, thermal optical properties, and thermal and electrical conductivity was observed by Verma *et al.* for the multiwalled CNT-PVA composite when compared to the pure thermally controlled PVA coating using the dip coating method (at 200 °C, 2 h) on aerospace alloys.[14] The GO-PVA composite was also found to have remarkable tribological properties in comparison to the pure PVA and graphene oxide coating.[15] Mechanical and tribological studies have been previously conducted on a fluorinated ethylene propylene polymer coated with stainless steel. Results showed that the FEP coating has excellent mechanical properties (hardness (57 GPa) and Young's modulus (1.56 GPa)), high adhesion, good scratch resistance, and tribological, corrosion resistance. Increased wear volume, low friction coefficient and low wear coefficient (3.1×10^{-4} mm^3 Nm^{-1}) were also observed in the FEP coating deposited by the spray process.[16] A study of the tribological properties of PVA with *Uncaria gambir* extract by heat treatment has been reported. Results showed improvement in the tribological properties, thermal properties, a reduced COF, enhanced wear rate and hardness, and a reduced coefficient of friction (0.08) compared to that of the pure PVA (0.26) using the ball-on-disk test.[17] A study of the mechanical, electrical, thermal and tribological properties of PVA with multiwalled graphene, CNT was performed by J. Joseph *et al.*[18] The results showed enhanced hardness, better wear resistance and reduced coefficient of friction (COF), reduction in the thermal stability, and improvement in the optical property (electromagnetic interference shielding effectiveness).

In understanding the properties and determination behaviour for a diverse range of materials and their applications, computational modelling and simulations are unique techniques that can complement experimental studies.[19] To assist the experimental outcomes and develop coatings with tuned features and functionalities, *in silico* approaches have increasingly been applied by researchers, scientists, and engineers in the modern research era.[20,21] For example, the structural, optoelectronic, mechanical, magnetic, anti-microbial, anti-icing, and adhesive properties, and the anti-corrosion performance are all directly affected at the atomistic/molecular level by coating particles, and by the interfacial interaction between two coating matrix/components (including the surface), which can effectively be determined using various computational tools. Importantly, resources and time can also be saved by these tools based on computational modelling approaches for the design and construction of new products.[22,23]

While some of the previously listed studies have reported on the mechanical and tribological behaviours of electrodeposited PVA-graphene/CNT coatings, these observations involving carbonaceous reinforcements and metals in the PVA polymer matrix are conspicuously absent from the literature. Studies based on scratch resistance investigations of polymeric composite coatings are lacking in the literature. In this work, the strength and bonding of PVA were increased by creating a synergistic effect of metallization (using nickel metal) and carbonaceous reinforcement encapsulation in the PVA matrix. This study explores the mechanical and tribological aspects (using micro-scratching for the first time on polymeric coatings) of electrodeposited PVA, along with Ni and carbonaceous reinforcements like carbon nanotubes (CNT), graphene (Gr), and diamond (D). The experimental wear values were linked through the theoretical tribological parameters using various models. As per the literature, no computational studies have been reported hitherto on the novel PVA-Ni-based composites using three different carbonaceous materials components, including diamond (with and without hydrogen atoms), CNT, and Gr. In this work, the interaction between the transition metal (Ni)-doped PVA and carbonaceous materials has great importance. In particular, there appears to be significant metal-nonmetal bonding interaction. This novel and unique feature motivated us to computationally examine the structural, stability, and electronic properties of such composite materials (PVA-Ni-D, PVA-Ni-CNT, PVA-Ni-Gr) for the first time. Quantum chemical calculations were performed using molecular modelling and electronic structure calculations approaches with density functional theory (DFT). The results from the mechanical, tribological, interfacial interaction calculations and computational studies demonstrated the enhanced strength and bonding for the diamond-containing PVA-Ni composite coating, which is attributed to a synergistic effect of metallization and carbonaceous reinforcement, and can be a potential material for a range of applications mainly in the marine, automotive, aerospace and electronics industries.

2. Materials and methods

2.1. Electrodeposition of coatings

The metallization of polymer coatings was done by adding nickel metal in the polyvinyl alcohol (PVA) suspension for elec-

trodeposition of the coatings. Initially, a clear aqueous PVA solution weighing 0.8 g l^{-1} was produced by dissolving polyvinyl alcohol in deionized water at a temperature of 90 °C while stirring. The PVA-Ni coating was fabricated using a Watt's bath (bath I, Fig. 1) containing a PVA mixture in the aqueous solution of $NiSO_4{\cdot}7H_2O$ (200 g l^{-1}), $NiCl_2{\cdot}6H_2O$ (40 g l^{-1}) and additives (such as 40 g l^{-1} boric acid, 5 g l^{-1} saccharin, and 2 g l^{-1} sodium dodecyl sulphate) in the electrolyte. The composite coatings were subjected to electrodeposition for one hour at 55 °C, pH 5, and 8 A dm^{-2} current density. Nickel plate served as the anode or counter electrode, and a mechanically polished stainless-steel plate served as the cathode or working electrode. When boric acid is absorbed on the cathode during electrophoretic deposition, it forms nickel borate, which increases the Ni^{2+} deposition potential, increases the hydrogen overpotential, and reduces the emergence of H_2 during electrophoretic deposition.[24,25] Also, on the cathode with the least amount of surface pitting, the sodium dodecyl sulphate improved the reduction of nickel. A surface area of 1 cm^2 was used for the electrodeposition, with Teflon tape covering the remaining region of the working electrode. For the uniform dispersion of particles, the electrolytic cell was placed on an Eltek Digimag M3D model magnetic stirrer spinning at 250 rpm. Moreover, to improve the mechanical characteristics, refine the microstructure, and improve the surface morphology of the PVA-Ni coatings, carbonaceous allotropes (carbon nanotubes: CNT, graphene: Gr, and diamond: D) were added separately to the electrolyte with the concentration of 0.5 g l^{-1} for both CNT (bath II, Fig. 1) and Gr (bath III, Fig. 1) and 10 g l^{-1} for diamond powder (bath IV, Fig. 1).[9,26] The carbon nanotubes (95% purity, 30–50 nm diameter), graphene nanoparticles (xGnP® grade H with an average thickness of approximately 15 nm) and diamond powder (3 μm size) were procured from Nanostructured and Amorphous Materials Inc., U.S., XG Sciences Inc., U.S., and Dev Tech India Pvt. Ltd, Maharashtra, respectively. Thus, by adding nickel and carbonaceous allotropes, four types of coatings were prepared by the electrodeposition process. These four coating types are represented in the schematic in Fig. 1 and named as PVA-Ni, PVA-Ni-CNT, PVA-Ni-Gr and PVA-Ni-D.

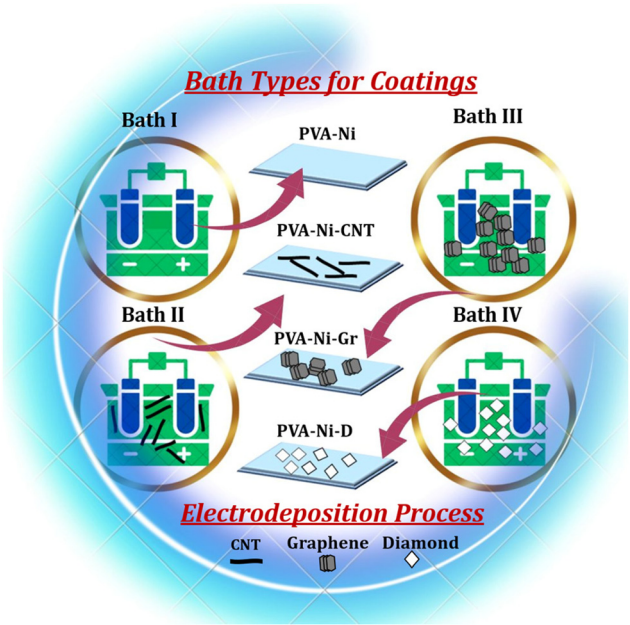

Fig. 1 Schematic representation of the bath types used in the electrodeposition process of the PVA-Ni, PVA-Ni-CNT, PVA-Ni-Gr and PVA-Ni-D composite coatings.

2.2. Microstructural, elemental, and phase characterizations

Electrochemically produced PVA-Ni, PVA-Ni-CNT, PVA-Ni-Gr and PVA-Ni-D coatings were examined for top surface morphology and chemical elemental analysis using a scanning electron microscope (JEOL-JSM-6010LA). The surface roughness of the composite coatings was observed through a surface profilometry test. Furthermore, to determine the presence of diamond, CNT, and graphene in the PVA-nickel matrix, Raman spectroscopy (Princeton Instruments, STR Raman, TE-PMT detector) was utilized in the backscattering mode with a 633 nm wavelength of a He–Ne red laser. The accumulation time and exposure duration were 15 and 25 seconds, respectively.

2.3. Mechanical property evaluation

A material's resistance to surface deformation, such as scratches and indentations, is measured by its hardness. It gauges a material's resistance to localized plastic deformation or piercing by a sharp object. Hardness gives information on the resistance to wear and abrasion. Hardness may be measured using a variety of techniques, including the pendulum, Brinell, Vickers, and Rockwell tests. The tensile strength and hardness of steel are approximately proportionate. It is crucial to remember that the tensile strength and hardness are two separate mechanical attributes that describe various facets of the behaviour of the material under various forms of mechanical stress.[27] The depth of an indenter's penetration under a heavy load, concerning the preload's penetration, is measured by the Rockwell test. The scale name and the HRC symbol are used to denote the hardness number. A 300*g* force on the coatings was used to measure the hardness.[28]

2.4. Tribological property evaluation

The electrochemically fabricated PVA-Ni-based composite coatings were scratched using a spherical Rockwell indenter with a 100 μm tip radius and an Instrumented Micro-indentation scratch tester from CSM International. The abrasive phenomena of the materials are influenced by the indenter geometry. Work hardening causes an increase in the hardness and wear resistance for a spherical indenter. While some ploughing and plastic deformation occurs, it is not as much as that produced by the work-hardening mechanism. The increase in hardness brought on by work hardening, however, is insufficient to boost the abrasion resistance when utilizing a conical indenter.[29] Therefore, metal composites are scratch-tested using a

Rockwell spherical indenter. Strain hardening of the surface layers may result from increased applied load. However, beyond a certain point, the wear rates for all coating systems increase linearly with applied load because higher loads remove the coating's topmost surface, exposing the surface below it to the counter body.[30] On the upper surface of the electrodeposited coatings, a 1 mm scratch length was created by applying a constant normal load of 10 N at a transverse speed of 12 mm min^{-1}.[31]

2.5 Computational studies

In this work, four cases have been taken by choosing three components-based composite models. Two composite models related to the diamond (two types, one with and one without H atoms) as PVA-Ni-D (with and without H), one PVA-Ni-CNT, and one PVA-Ni-Gr have been modelled to gain new insights into their structural stability in terms of the energetics and electronic features. The optimization and frequency calculations for the computationally probed systems (components and composite models) were performed using the quantum chemical calculations approach in the framework of the electronic structure calculations package Gaussian 09.[32] After the optimization process was performed for all systems, all frequencies were detected to be positive, which showed that the systems are all stable. The DFT approach using the functional B3LYP and basis set 6-31G was applied for all computationally inspected systems.

3. Results and discussion

3.1. Microstructural and phase analysis of the composite coatings

The scanning electron microscopic, surface profilometric and EDS images of the electrodeposited PVA-Ni and PVA-Ni-carbonaceous coatings can be observed in Fig. 2. The surface mor-

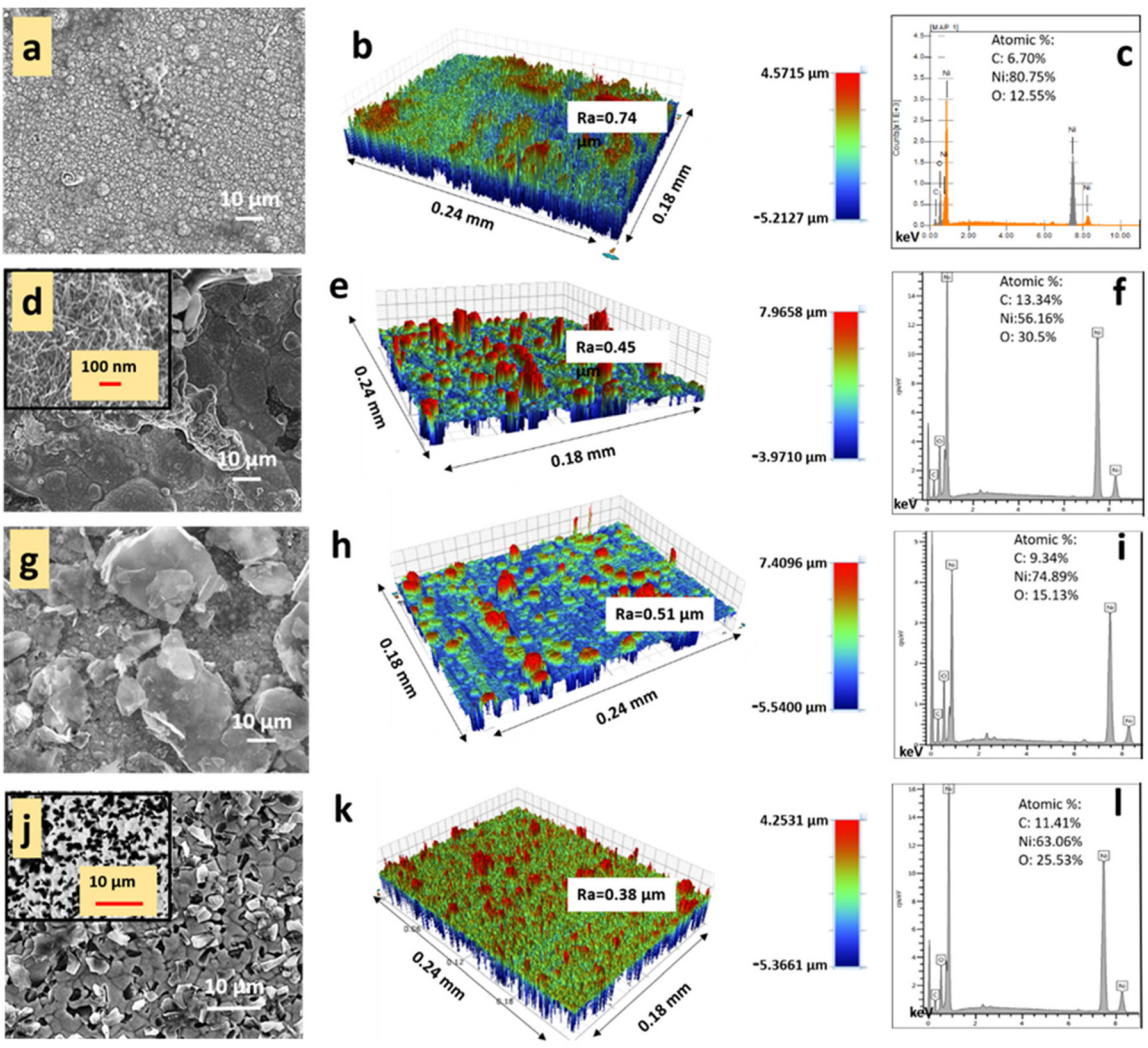

Fig. 2 Scanning electron microscopic, surface profilometry images and EDS spectra, respectively, for the (a, b and c) PVA-Ni, (d, e and f) PVA-Ni-CNT (inset at high magnification), (g, h and i) PVA-Ni-Gr, and (j, k and l) PVA-Ni-D (BSE mode at inset) composite coatings.

phology of the PVA-Ni coating (Fig. 2a) is smooth without any additive features in the coating, while the dispersed CNTs and graphene can be clearly detected from the PVA-Ni-CNT and PVA-Ni-Gr coatings (Fig. 2d and g). The insets of the corresponding figures show the high-magnification images of CNTs and graphene. The PVA-Ni-D coating (Fig. 2j) exhibits the well-dispersed diamond particles, and the backscattered electron mode of the image of dispersed diamond particles is given in the inset. The similar SEM images of PVA indicated that the nanofillers have excellent adhesion and interfacial bonding to the PVA matrix with a positive effect on the mechanical strength due to the strong interfacial interaction, as reported by Hajeeassa *et al.*[33] Furthermore, as there are no papers available on metallization- and carbon allotrope-incorporated PVA coatings, a comparison was made using the PVA-MGr-CNT composite coatings.

The surface profilometric images for the composite coatings revealed a sharply decreased roughness (R_a 0.38 μm) for the PVA-Ni-D coating (Fig. 2k) compared to that of PVA-Ni (R_a 0.74 μm, Fig. 2b), agglomerated PVA-Ni-CNT (R_a 0.45 μm, Fig. 2e) and PVA-Ni-Gr (R_a 0.51 μm, Fig. 2h) composite coatings. The reduced surface roughness in PVA-Ni-D was due to the better dispersion of diamond particles. Additionally, the energy-dispersive X-ray spectroscopy (EDS) measurements of the samples demonstrated the existence of C, O, and Ni elements (Fig. 2c, f, i and l) for all coatings due to the occurrence of PVA, Ni, and carbonaceous allotropes.[34,35] No other peaks can be seen in the EDS spectrum, which illustrates that no impurity was generated during the deposition of the coatings.

Furthermore, each composite sample was studied *via* Raman spectroscopy to confirm the presence of carbon nanotubes, graphene, and diamond in the PVA-Ni matrix (Fig. 3). The PVA-Ni coating shows Raman peaks at ~1410 cm^{-1} and ~1620 cm^{-1} due to two-phonon (2P) and two-magnon (2 M) light scattering, respectively, for Ni. However, for the PVA-Ni-Gr coatings and PVA-Ni-CNT, the distinctive bands of graphene and CNT were found, contributing to a D-band (at 1355 cm^{-1}), G-band (at 1580 cm^{-1}), and 2D-band (at 2690 cm^{-1}). Furthermore, the PVA-Ni-D coating exhibited a distinctive sharp peak for diamond (disorder-generated D-band sp^3 hybridized carbon atoms) at around 1333 cm^{-1}, devoid of any combination of graphitic-induced sp^2 hybridized G-band. This suggests an appropriate dispersion and high-quality coating of PVA-Ni-D.

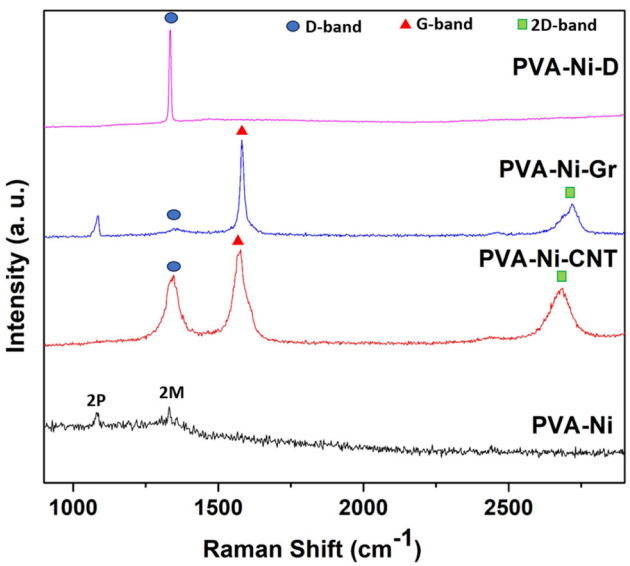

Fig. 3 Raman spectra of the PVA-Ni, PVA-Ni-CNT, PVA-Ni-Gr and PVA-Ni-D composite coatings.

3.2 Mechanical and tribological properties investigations

A Rockwell hardness tester was used to assess the mechanical strength of the coatings. The results showed that the PVA-Ni-D coating had the maximum hardness (59 HRC), which allowed it to bear the load more substantially (Table 1). The hardness was reduced comparatively for the PVA-Ni (33 HRC), PVA-Ni-CNT (48 HRC) and PVA-Ni-Gr (44 HRC) composite coatings. In the current work, metallization and addition of carbonaceous reinforcements in the PVA matrix remarkably increased the mechanical performance of the composite coatings when compared to the previous work reported on PVA coatings.[36] The previous literature completely lacks the scratch testing of any polymeric coatings and the current work reported first-time scratch analysis of polymer-based composite coatings. The results from a tribological investigation using micro-scratch testing divulge that the coefficient of friction value for PVA-Ni-D coating is minimum (0.37), however for the other coatings, it starts to rise and approaches 0.48, for instance, COF for PVA-Ni, PVA-Ni-CNT, PVA-Ni-Gr were 0.48, 0.45, 0.44, respectively (Fig. 4).

Furthermore, from eqn (1), following micro-scratching testing, the scratch wear volume (W_v) of the coatings was deter-

Table 1 Characterization of the electrodeposited materials via scratch testing

Samples	Hardness (HRC)	Scratch COF (μ)	Penetration depth h_p (μm)	Residual depth h_r (μm)	Scratch width (μm)	Scratch hardness (GPa)	Scratch wear volume (10^{-5} mm^3)	Scratch wear rate (10^{-3} mm^3 Nm^{-1})
PVA-Ni	33	0.48	26.6	16.3	122.67	1.72	10.29 ± 0.25	10.29 ± 0.25
PVA-Ni-CNT	48	0.45	23.9	17.2	86.44	3.45	8.18 ± 0.16	8.18 ± 0.16
PVA-Ni-Gr	44	0.44	23.4	15.1	94.15	2.89	8.65 ± 0.21	8.65 ± 0.21
PVA-Ni-D	59	0.37	19.2	13.4	72.29	4.92	7.34 ± 0.17	7.34 ± 0.17

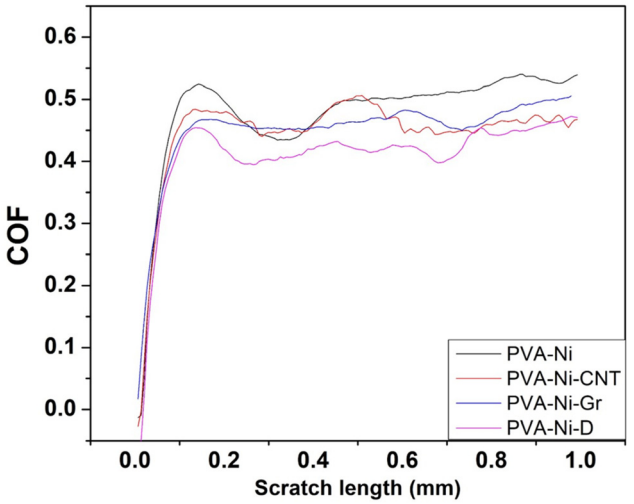

Fig. 4 Graph of the coefficient-of-friction and scratch length at 10 N load during the scratching of the PVA-Ni, PVA-Ni-CNT, PVA-Ni-Gr, and PVA-Ni-D composite coatings.

mined using the scratch length (L), indenter radius (R), and penetration depth (h_p).[37,38]

$$W_v = L\left[R^2 \arccos\left(1 - \frac{h_p}{R}\right) - (R - h_p)\sqrt{2Rh_p - {h_p}^2}\right] \quad (1)$$

Additionally, the wear volume (W_v), force (F, 10 N), and scratch length (1 mm) were used to compute the wear rate.[39]

$$W_R = \frac{W_v}{FL} \quad (2)$$

The PVA-Ni coating has a high wear volume of 10.29×10^{-5} mm^3 when compared to that of the PVA-Ni-CNT (8.18×10^{-5} mm^3), PVA-Ni-Gr (8.65×10^{-5} mm^3) and PVA-Ni-D (7.34×10^{-5} mm^3) carbonaceous coatings. Consequently, it was found that adding carbonaceous reinforcements to an electrolytic solution results in a lower COF and wear volume, which leads to increased wear resistance compared to other coatings. The depth profile (Fig. 5) illustrates how deeply the coatings penetrate. For the PVA-Ni-D coating, it can be observed that the penetration depth is the minimum value (19.2 μm). Thus, the usual penetration profile is more uniform because of the coating's smooth and flat surface in contrast to those of the PVA-Ni, PVA-Ni-Gr, and PVA-Ni-CNT coatings, which all have cracked, delaminated surfaces (Fig. 5 and Table 1).

The measurement of the coatings' resistance to normal penetration can be computed using the width of the scratches (d) and applied load (F) to get the scratch hardness (H_s) *via* the following equation:[40]

$$H_s = \frac{8F}{\pi d^2} \quad (3)$$

In the PVA-Ni-D coating, a decreased scratch width (72.29 μm) was observed (Fig. 6), which demonstrated a higher scratch hardness (4.92 GPa) and greater resilience to the applied force. As shown in Fig. 6, the end portion of the micro-scratch and enlarged view within the scratches demonstrate that the PVA-Ni-D coating has venerable wear resistance without chipping, delamination, cracking, or loss of surface cohesiveness (Fig. 6d, h and Table 1). A smoother scratch track surface is grafted onto PVA-Ni-D. Conversely, the PVA-Ni coating exhibits cracks, grooves, and delamination on the scratch surface as a result of direct interaction between the indenter and the coating's upper surface. Moreover, the PVA-Ni-CNT and PVA-Ni-Gr coatings exhibit similar surface structures with comparatively less scratch width and damaged surface from PVA-Ni, but higher width and cracked surface from PVA-Ni-D. The main mechanism for such type of wear of coatings was presumed to be 2-body abrasion wear. There were some mild abrasive wear lines visible in the sliding direction on the scratched surface. This type of wear is caused by debris that is created during sliding and becomes caught between the coated surface and the indenter, resulting in micro-ploughing due to 2-body abrasion.[41,42]

3.3 Models to compare the theoretical values with the coatings' experimental wear and friction behaviour

The experimental tribological parameters of the PVA-based composite coatings were compared with the theoretical values of depth and pressure. To appraise the wear performance of the polymeric coatings theoretically, some reported models are implicated.[43]

$$h_c = \frac{h_p + h_r}{2} \quad (4)$$

$$a = \sqrt{2Rh_c - {h_c}^2} \quad (5)$$

$$p_c = \frac{F}{\pi a^2} \quad (6)$$

The extent of contact between the coated surface and the indenter can be explained by the following three parameters, contact depth (h_c), contact radius (a), and contact pressure (P_c), which can be computed using the penetration depth (h_p), residual scratch depth (h_r), applied force (F), and indenter radius (R). For the PVA-Ni-D coating, the lowest value of contact for depth (16.3 μm) and contact radius (54.8 μm) with an increased value of contact pressure (1.07 GPa) was obtained. Meanwhile, the maximum contact depth, contact radius and reduced contact pressure were calculated for PVA-Ni (Table 2). These values are almost similar in the case of PVA-Ni-CNT and PVA-Ni-Gr, which show the damaged surfaces in the PVA-Ni, PVA-Ni-CNT and PVA-Ni-Gr coating.

The friction mechanism of the scratch formed during testing can be explained by two domains. In the coefficient of friction (COF), there are two parameters to be considered: the initial parameter is the ploughing COF, which has a low load scratch, showing the plastically deformed surface of the composite with damage at both ends of the groove. The second parameter is adhesive COF, which has an increasing load and comprises micro-cutting grooves. These parameters of COF

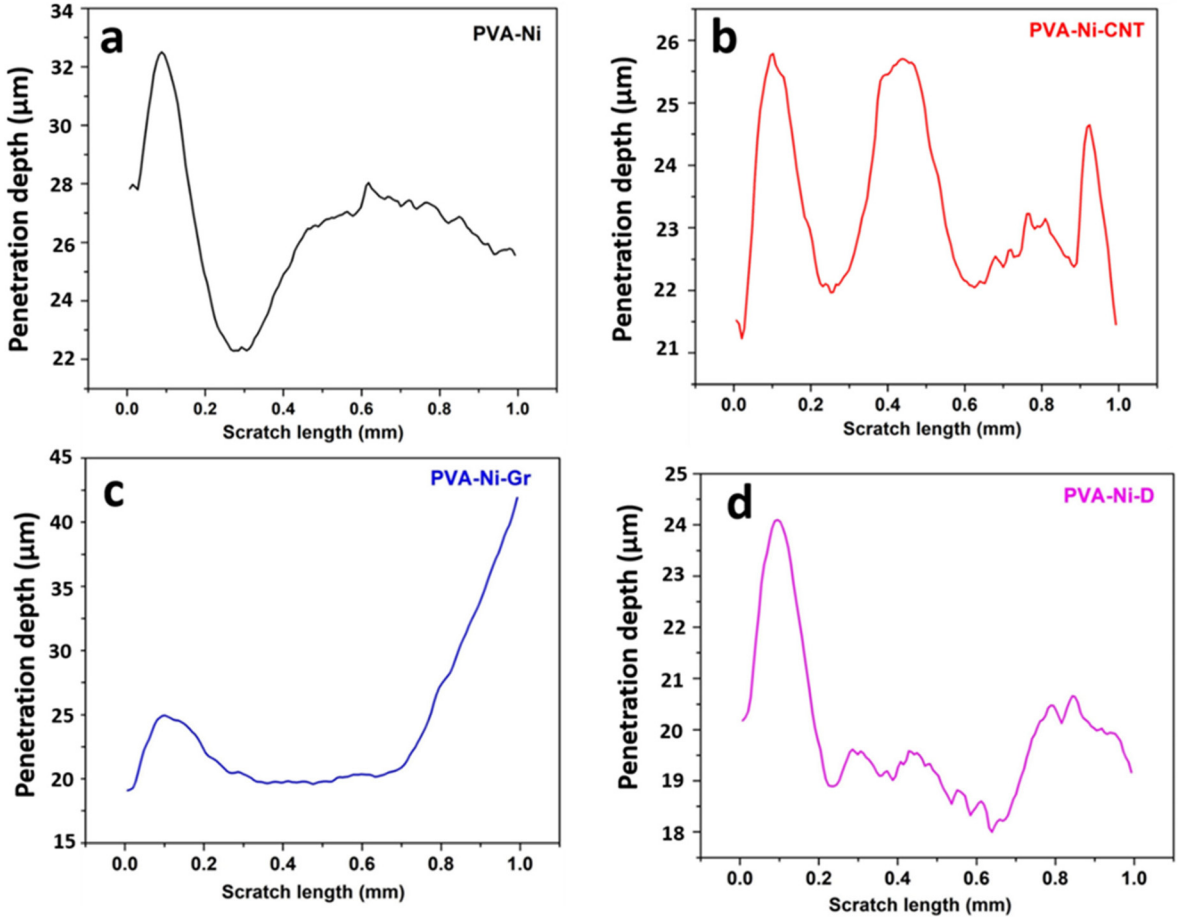

Fig. 5 Depth profile during the micro-scratching of the (a) PVA-Ni, (b) PVA-Ni-CNT, (c) PVA-Ni-Gr, and (d) PVA-Ni-D composite coatings.

were reported by Venkatachalam *et al.*[44] and Xiao *et al.*,[45] and can be defined as follows:

$$\mu = \mu_a + \mu_p. \tag{7}$$

The following is an expression for the ploughing friction coefficient:

$$\mu_p = \frac{4a}{3\pi R} \tag{8}$$

here, μ_a is the friction coefficient of adhesion, μ_p is the friction coefficient of ploughing, and R is the indenter radius. The PVA-Ni-D coating's improved wear resistance with a lower ploughing and adhesion coefficient-of-friction (0.23 and 0.13, respectively) were also indicated by the estimated sub-parameters of the COF. In contrast, PVA-Ni, PVA-Ni-CNT, and PVA-Ni-Gr exhibit more wear resistance with bigger COF (0.48), ploughing COF (0.26 and 0.25, 0.25, respectively), and adhesion COF (0.21 and 0.19, 0.18, respectively). A model pertaining to the normal force on the surface and the tangential force (F_x) on the tip during the scratch testing was put out by Benjamin and Weaver.[46] Three components make up the model associated with the tangential force: a ploughing force that can push away the detached film, a force that can peel the coating off the substrate, and a force that can distort the substrate. The model has many parameters, including scratch width (d), indenter radius (R), substrate and coating hardness (H_c and H_s), coating thickness (t), and shear stress (τ) at the coating-substrate interface.

$$F_x = \frac{d^3}{12R}H_s + \frac{\pi}{4}\tau d^2 + dtH_c \tag{9}$$

However, the measurements of the metal coatings on the glass substrate did not correlate well with this concept. Consequently, a second model utilizing the substrate hardness and contact radius (a) was presented by Benjamin and Weaver[46] in relation to the shear stress at the indenter's tip (τ_s).

$$\tau_s = \frac{H_s a}{\sqrt{R^2 - a^2}} \tag{10}$$

This theoretical model was a standard model used to give approximative data on the coating adherence. Eqn (4) was utilized to derive the contact radius (a, Table 2) in this model, which was employed to test the adhesion. The substrate's hardness of 2.4 GPa was acquired from the literature.[47] Compared to the PVA-Ni coating (1.89 GPa) and CNT, gra-

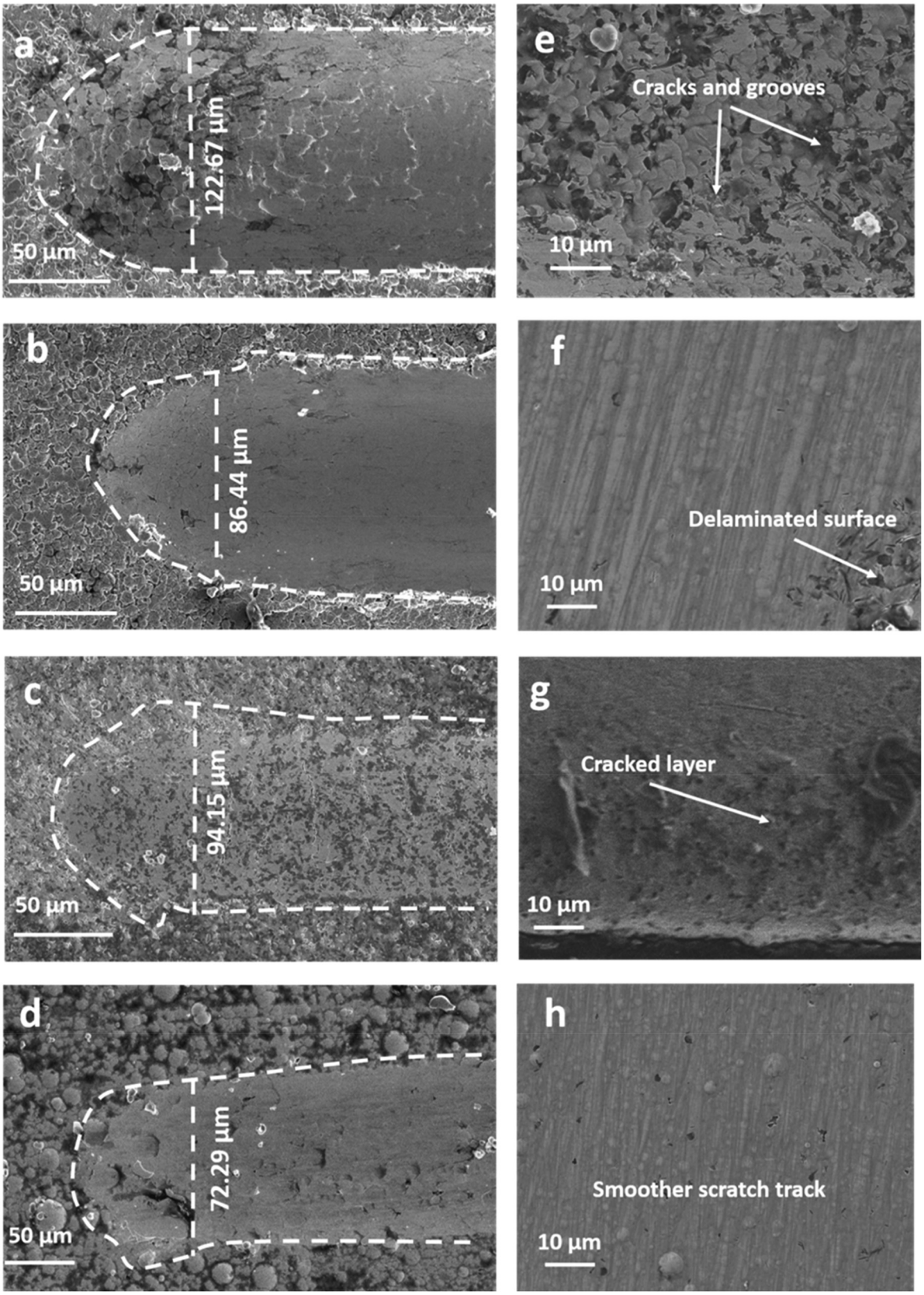

Fig. 6 End parts of the micro-scratched samples (a, b, c and d) and assessment of the enlarged portions within the scratch (e, f, g and h), respectively, for the PVA-Ni, PVA-Ni-CNT, PVA-Ni-Gr and PVA-Ni-D composite coatings.

Table 2 Calculating the amount of contact between the surface of the electrodeposited samples and the scratch indenter

Samples	h_c (μm)	a (μm)	P_c (GPa)	μ_p	μ_a	τ_s (GPa)
PVA-Ni	21.4	61.9	0.83	0.26	0.21	1.89
PVA-Ni-CNT	20.6	60.8	0.86	0.25	0.19	1.83
PVA-Ni-Gr	19.3	59.0	0.91	0.25	0.18	1.75
PVA-Ni-D	16.3	54.8	1.07	0.23	0.13	1.56

phene-added coatings, PVA-Ni-D exhibits the lowest shear stress and, consequently, the highest adhesion strength with the substrate (1.56 GPa) (Table 2).

3.4 Discussions based on the interfacial interactions of the composite coatings

Furthermore, the mechanical characteristics of the composites are significantly influenced by the interface between the matrix and reinforcements, which is contingent upon the geometry of the reinforcements. The volume percentage and efficient surface area per unit volume of the reinforcements (α), which may be computed using the following relations, provide the basis for an explanation of the interfacial interaction.[24]

$$\alpha_D = \frac{S_D}{V_D} = \frac{4\pi\left(\frac{d_D}{2}\right)^2}{\frac{4}{3}\pi\left(\frac{d_D}{2}\right)^3} = \frac{6}{d_D} \quad (11)$$

$$\alpha_{CNT} = \frac{S_{CNT}}{V_{CNT}} = \frac{\pi d_{CNT} l_{CNT} + 2\frac{\pi {d_{CNT}}^2}{4}}{\pi\frac{{d_{CNT}}^2}{4} l_{CNT}} = \frac{2(2\delta_{CNT}+1)}{l_{CNT}} \quad (12)$$

$$\alpha_{Gr} = \frac{S_{Gr}}{V_{Gr}} = \frac{\pi d_{Gr} t_{Gr} + 2\frac{\pi {d_{Gr}}^2}{4}}{\pi\frac{{d_{Gr}}^2}{4} t_{Gr}} = \frac{2(2+\delta_{Gr})}{d_{Gr}} \quad (13)$$

where the subscripts D, CNT, and Gr stand for the diamond, carbon nanotube, and graphene reinforcements, respectively, and d, l, t, and δ for the diameter, length, thickness, and aspect ratio of the reinforcements. Due to the non-functionalization of CNT and graphene, they cannot make strong chemical bonds with the matrix and therefore, could not offer strong interfacial anchoring. Due to particle–particle interaction (higher volume % and α of CNT and graphene, Table 3), the enhanced reinforcement interface[48] of CNT and graphene results in a reduction in the mechanical and tribological values (Table 1) relative to diamond. Furthermore, because of their larger surface areas, the lubricating graphitic properties of graphene and CNT tend to adhere to the particles when they are loaded, making the particle sliding easier. They also do not help to prevent matrix deformation. Conversely, because of the larger size (3 μm), the stiff sp^3 network of the diamond resists matrix deformation and has a strong mechanical interlocking (particle-matrix interaction) with the matrix.

4. Computational results and discussion

A range of *in silico*-based studies can be seen in the reports, where diverse kinds of structural, stability/energetics, and electronic features have been reported.[49] Importantly, the highest occupied molecular orbital (HOMO) and lowest unoccupied molecular orbital (LUMO) are the Frontier molecular orbitals (FMOs), which show the properties related to the bulk and surface states, respectively, along with taking care of the HOMO–LUMO gap (E_{gap}) showing the optoelectronic features, including singly occupied molecular orbital (SOMO) in some cases. Fig. 7 demonstrates the optimized/equilibrium structures of five component models (PVA, Gr, D with and without H, CNT) and one Ni-based PVA composite model. Some important and chosen Ni–O and Ni–C bond lengths for the PVA-Ni and all four PVA-Ni-carbonaceous moieties-based composite models can be discerned from Table 4. The bond length between the O atom of the PVA and Ni metal has been calculated as 1.796 Å. Moreover, it is important and interesting to note that all composite models have been designed by keeping in mind the experimental facets where the transition metal (Ni)-allied with the PVA was anchored with the D (with and without H atoms), Gr, and CNT, separately using the molecular modelling approach, followed by electronic structure calculations approaches.

The optimized structures of all four composite models are displayed in Fig. 8. First having a look into the Ni–O metal-nonmetal bond length of the PVA-Ni-D (with and without H), the Ni–O bond distances for both composite models (ranging from 1.828 Å to 2.195 Å) have been found to be greater than the PVA-Ni composite model (1.796 Å), as expected. A similar trend for the Ni–O bond lengths (see Table 4) can be seen for the other two composite models (PVA-Ni-Gr and PVA-Ni-CNT),

Table 3 The reinforcements' geometrical features and properties

Reinforcements	Area (D band of Raman spectrum)	Total area	Theoretical vol % (area of D band/total area)	Geometric parameters	Aspect ratio (δ)	α
CNT	90 598.7065	330 385.8	15	d_{CNT} = 40 nm l_{CNT} = 15 μm	375	0.100
Gr	28 809.6855	187 986.9	27	d_{Gr} = 15 μm t_{Gr} = 15 nm	1000	0.133
D	4 672 270.00	41 800 000	11	d_D = 1.5 μm	1.5	0.004

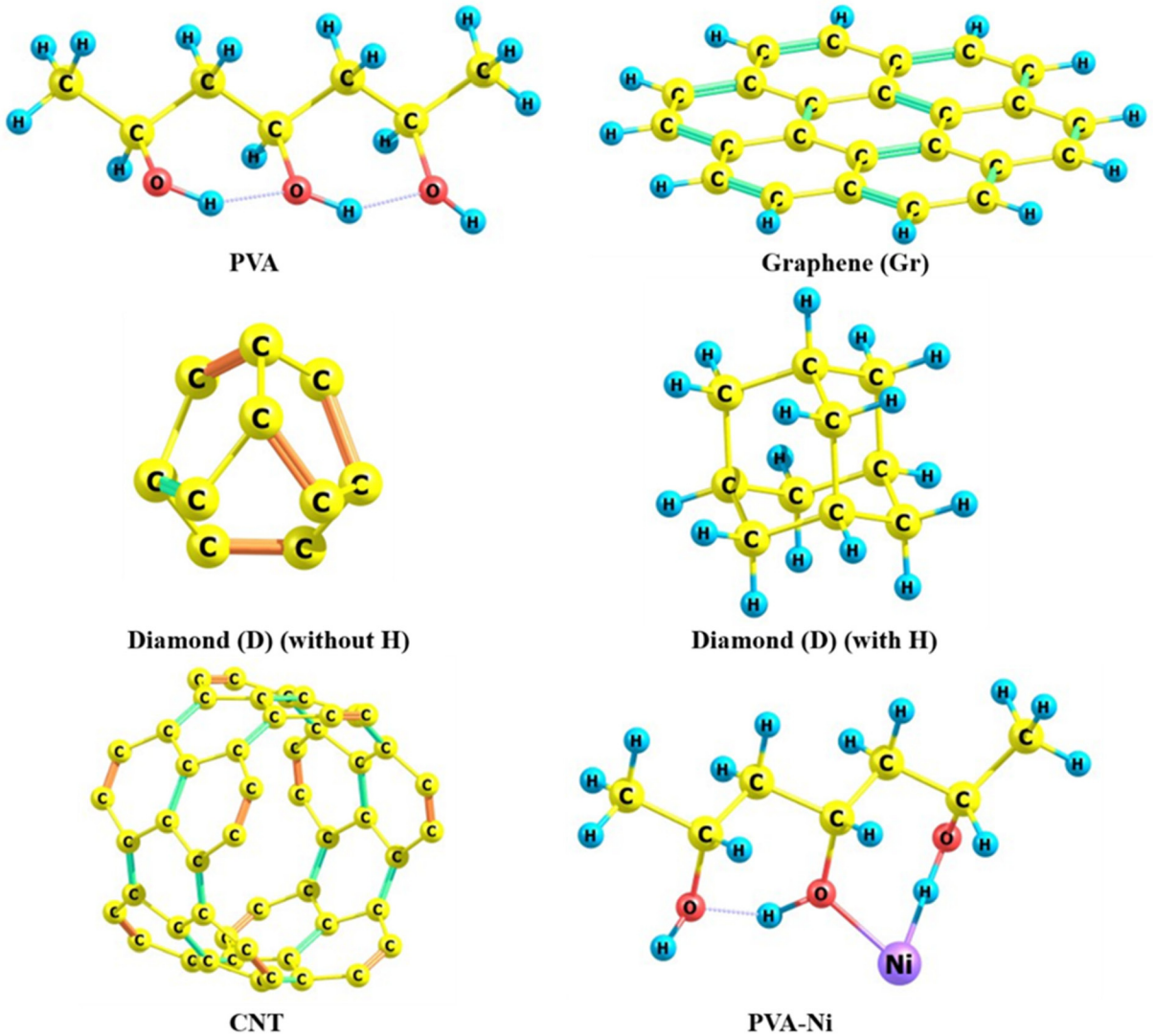

Fig. 7 Optimized structures of the PVA, graphene (Gr), diamond-D (without and with H), CNT component, and PVA-Ni composite models.

Table 4 Some selected and important geometrical (metal-nonmetal bonding) parameters of the Ni-doped PVA (PVA-Ni) and four composite models [PVA-Ni-D (with and without H atoms), PVA-Ni-CNT, and PVA-Ni-Gra] at the B3LYP/6-31G level of approach

	Composite models (trimer complex)		
PAM-Ni-CNT	PVA-Ni-D (without H)	PVA-Ni-D (with H)	PVA-Gra
Metal–nonmetal bond Ni27–O14 (1.909 Å) Ni27–C58 (1.856 Å) Ni27–C49 (1.858 Å) Ni27–C40 (1.905 Å)	Metal–nonmetal bond Ni27–O14 (1.828 Å) Ni27–O10 (1.932 Å) Ni27–C32 (1.901 Å) Ni27–C28 (1.900 Å) Ni-allied PVA Composite Model (PVA-Ni) Ni–O (1.796 Å)	Metal–nonmetal bond Ni27–O10 (2.195 Å) Ni27–O14 (1.983 Å) Ni27–C52 (1.902 Å)	Metal–nonmetal bond Ni27–O14 (1.958 Å) Ni27–O10 (1.994 Å) Ni27–C31 (1.871 Å) Ni27–C32 (1.902 Å)

where the bond distances have been found to be larger (1.909 Å to for the PVA-Ni-CNT and 1.958 Å and 1.994 Å for the PVA-Ni-Gr systems) than that of the PVA-Ni composite (1.796 Å) alone. Such increased structural/geometric (Ni–O bond lengths) parameters clearly indicate the formation of the stable (more favourable) complex/composite, as expected in accordance with the supramolecular approach.

Importantly, the average intermolecular Ni–C bond lengths (a prime structural parameter) between the PVA-Ni component and the other components, carbonaceous materials, like D, Gr,

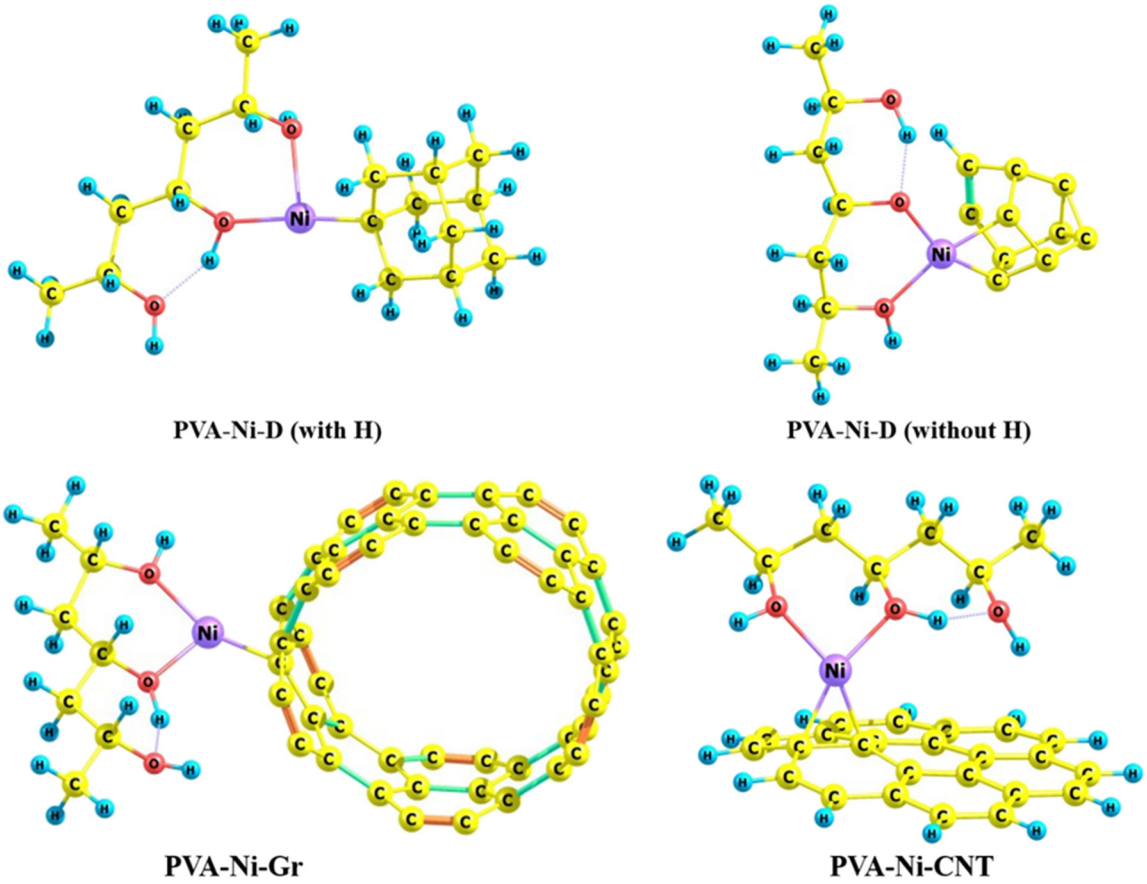

Fig. 8 Optimized structures of the PVA-Ni-D (with and without H), PVA-Ni-CNT, and PVA-Ni-Gr composite models.

and CNT, were calculated as 1.873 Å, 1.887 Å, and 1.901 Å for the PVA-Ni-CNT, PVA-Ni-D, and PVA-Ni-Gr, correspondingly, which give an indication of the significant interfacial metal-nonmetal (Ni–C) bonding interaction(s) that stabilize the complexes/composite models. Both kinds of intermolecular and influential metal-nonmetal interactions (Ni–C and Ni–O) appeared to be due to significant (d–p overlap) between the d-orbital of the Ni metal and p-orbital of the carbon framework of the carbonaceous-based components. The other imperative stabilizing parameters/factors are shown in Table 5.

Moreover, in gaining new insights into the binding interaction between the Ni metal of the PVA-Ni component and C atoms of the carbonaceous materials, the binding energy (BE) (in the presence of metal) has been calculated in the framework of the supramolecular approach.[50,51] In the case of the PVA-Ni-D composite model, a total of two cases, PVA-Ni-D (with H) and PVA-Ni-D (without H), have been considered here in this research work. It is astonishing to see that the BE was detected to be positive (gives an indication of endothermic reaction and thermodynamically unfavourable) with a large value (HF: 260.3 kcal mol^{-1} and DFT: 245.9 kcal mol^{-1}) for the

Table 5 Some chosen and useful electronic parameters of the Ni-doped component (PVA-Ni) and four composite models [PVA-Ni-CNT, PVA-Ni-Gra, and PVA-Ni-D (with and without H atoms)] at the B3LYP/6-31G level of theory

System	PVA-Ni-D (diamond without hydrogen)	PVA-Ni-D (diamond with hydrogen)	PVA-Ni-CNT	PVA-Ni-Gra
Binding energy (in kcal mol^{-1})	−271.7 (−257.4 HF/3-21G)	245.9 (260.3 HF/3-21G)	−136.5 (−122.2 HF/3-21G)	−67.1 (−52.7 HF/3-21G)
HOMO (in eV)	−5.434	−3.146	−4.406	−3.491
LUMO (in eV)	−3.478	0.460	−3.069	−0.797
HOMO–LUMO gap (in eV)	1.956	2.686	1.337	2.664
Dipole moment (in Debye, D)	7.7	11.6	8.5	15
Natural charge (e)	PVA-Ni (0.735) D (−0.735)	PVA-Ni (0.819) D (−0.319)	PVA-Ni (1.110) CNT (−1.110)	PVA-Ni (0.899) Gra (−0.899)

PVA-Ni-D (with H) composite model. However, notably, the BE value (HF: −257.4 kcal mol^{-1} and DFT: −271.7 kcal mol^{-1}) for the PVA-Ni-D (without H) has been analyzed to be the most negative (indicating an exothermic reaction and thermodynamically stable), and the highest among all other three composite models' cases [PVA-Ni-D (without H), PVA-Ni-CNT, and PVA-Ni-Gr]. The order of the BE (indicating the stability) is found to be PVA-Ni-D (without H) (HF: 257.4 kcal mol^{-1} and DFT: 271.7 kcal mol^{-1}) > PVA-Ni-CNT (HF: 122.2 kcal mol^{-1} and DFT: −136.5 kcal mol^{-1}) > PVA-Ni-Gr (HF: −52.7 kcal mol^{-1} and DFT: −67.1 kcal mol^{-1}), which is consistent with the experimentally observed parameters [penetration depth (h_p), scratch volume, and scratch hardness].

Very interestingly, by examining the HOMO–LUMO gap (E_{gap}) values of all four composite models, the order of the E_{gap} values is as follows: PVA-Ni-D (with H) (2.686 eV) > PVA-Ni-

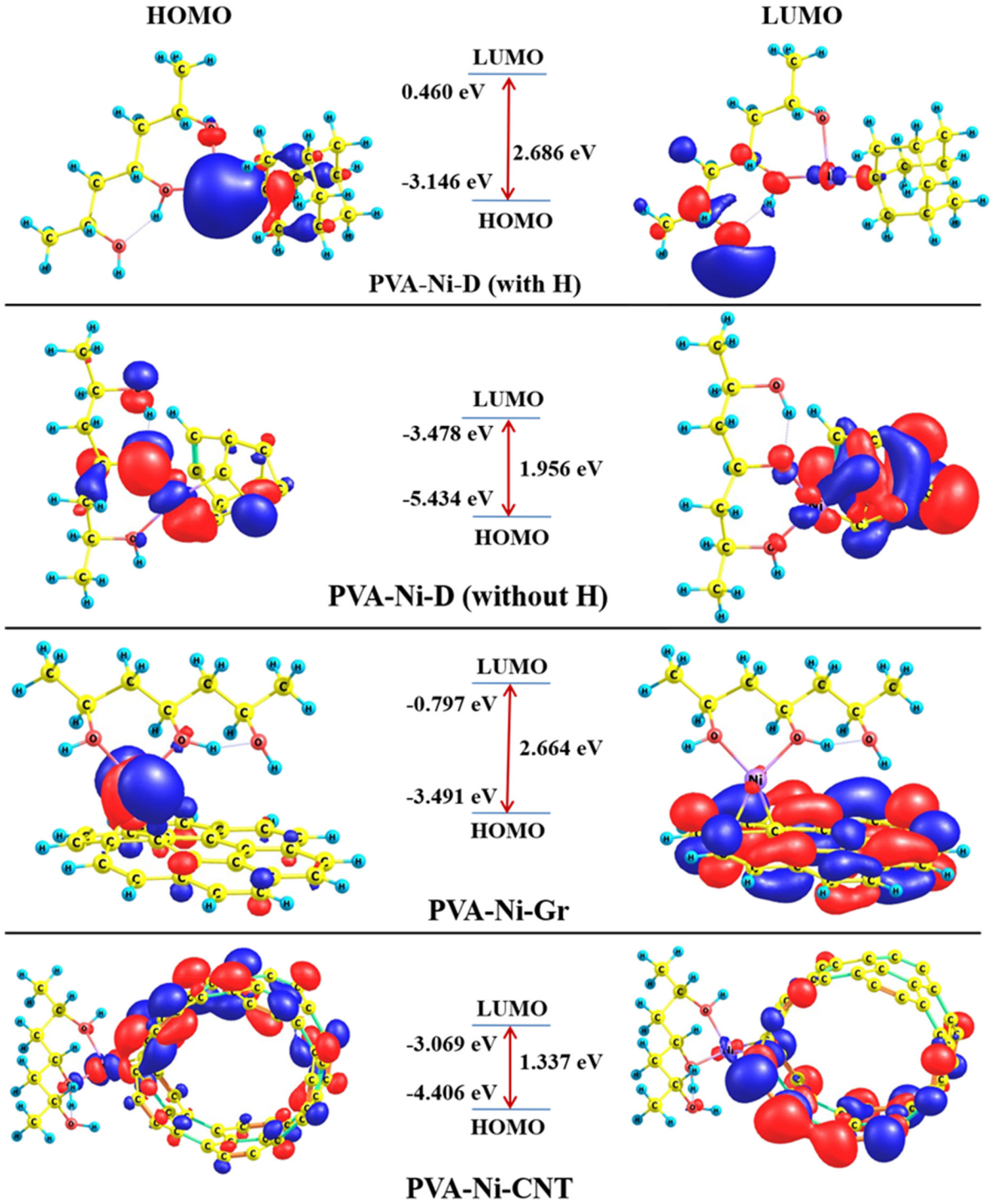

Fig. 9 HOMO and LUMO isosurface maps of the PVA-Ni-D (with H and without H), PVA-Ni-Gr, and PVA-Ni-CNT composite models.

Gr (2.664 eV) > PVA-Ni-D (without H) (1.956 eV) > PVA-Ni-CNT (1.337 eV). This clearly shows that the former PVA-Ni-CNT consisting of the lowest E_{gap} value has the highest tendency to excite the photoelectron from the HOMO to LUMO.[52] It should be noted that the E_{gap} of the PVA-Ni-D (without H) is smaller than that of the PVA-Ni-D (without H), which could be due to the exclusion of H in the D and involvement of delocalized pi-electrons therein. The above marked E_{gap} values clearly indicate that the D (without H) shows better optoelectronic properties (quick photoelectron excitation from the HOMO to LUMO level). The order of the dipole moments of the three species as shown in Table 5 has been computed as follows: PVA-Ni-D (without H) (7.7 Debye) < PVA-Ni-CNT (8.5 Debye) < PVA-Ni-Gr (15 Debye). This clearly indicates that PVA-Ni-D (without H) is the least reactive (the most stable) among all nanocomposites. Notably, as the charge transfer (CT) phenomenon plays an important role in several processes, Table 5 shows the highest charge (CT) between PVA-Ni (1.11e) and CNT (−1.11e) for the PVA-Ni-CNT composite model, which indicates that the CT takes place from PVA-Ni to the CNT component.[53] Very interestingly, a similar pattern can also be seen in all other composites, where the CT process occurs from PVA-Ni component to the carbonaceous components (see Table 5).

Now, let us closely examine the FMOs (HOMOs and LUMOs) of all probed composite models playing an important role in the photoelectron excitation (from HOMO to LUMO level).[54] The plotted three-dimensional (3D) isosurface maps of all species can be discerned from Fig. 9. The SOMO of the PVA-Ni-D (with H) appears to be spread over the N-metal and the HOMOs near the four C atoms of D (close to the Ni-metal), whereas the LUMOs are revealed to be located mainly over the two C and two O atoms of the PVA component. However, in the case of the PVA-Ni-D (without H) species, the HOMOs have been detected to be close to one O, two C, and the Ni atom of the PVA-Ni component, while the LUMOs are significantly spread over the C atoms of the D component. Interestingly, having a view on the PVA-Ni-Gr composite model, the HOMOs are distributed over the some of the C atoms of the Gr and the SOMOs are located on the Ni-metal atom of the PVA-Ni components. However, the LUMOs are spread over almost all C atoms of the Gr component. Finally, the HOMOs of the PVA-Ni-CNT system have been seen throughout the Ni metal and top segment of the CNT moiety, whereas the LUMOs are found to be near the lower fragment of the CNT component.

The combined effects of the volume fraction, surface roughness and reinforcement morphology on the strength (mechanical and tribological) and bonding performances of the electrodeposited Ni-PVA composite coating with diamond, carbon nanotube, and graphene reinforcement are discussed. The agglomerated (higher surface roughness of 0.45 μm) lubricating graphene's graphitic layers slide off from the matrix during micro-scratching, and CNTs responded in the same way because of their weak connection with the Ni-PVA matrix. Additionally, because of their small size (less than hundreds of nm), they become caught in the Ni-PVA matrix and are unable to limit their deformation (Table 3). However, by acting as the supporting structure, a comparatively bigger sized and well-dispersed (reduced surface roughness of 0.38 μm) diamond particle (~few μm) seems to limit the rotation or sliding of small grains (~tens of nm size). Therefore, the stronger protective coatings are produced by the improved particle strengthening of the electrodeposited Ni-PVA-D, rather than by CNT and graphene reinforcement. The synergistic effect of adding metal (Ni) and carbonaceous allotropes (diamond, CNT, and graphene) in the PVA matrix resulted in the strengthening with strong mechanical interlocking and bonding to the polymeric material. A schematic of the overall summary of the current work is presented in Fig. 10.

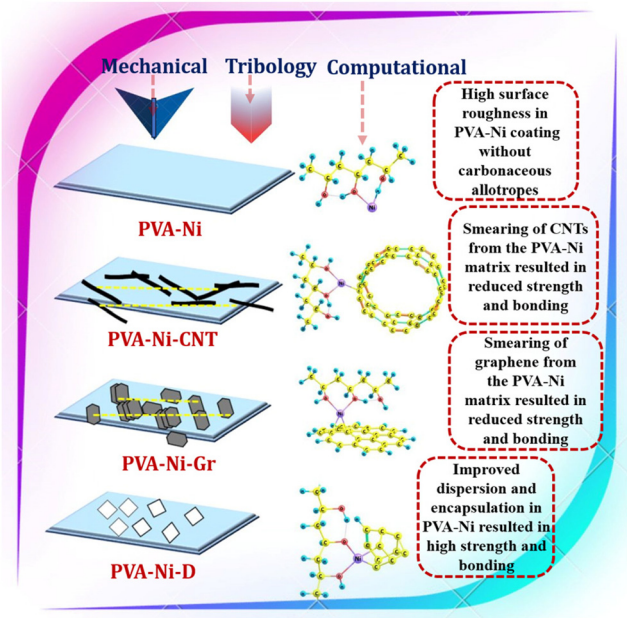

Fig. 10 Schematic showing a bird's eye view of the current work.

5. Conclusion

Electrodeposition was used to design composite coatings of PVA with the encapsulation of metal (nickel) and various carbonaceous reinforcements (graphene, carbon nanotubes, and diamond) to protect various engineering devices. Because of the synergistic effects of metallization and carbonaceous reinforcements, the mechanical strength and scratch wear volume of the coatings grafted with carbonaceous reinforcements decreased relative to that of PVA-Ni coating (from 10.29 × 10^{-5} mm^3 to 7.34 × 10^{-5} mm^3). Moreover, the mechanical and scratch testing prefer diamond as an adroit additive over graphene and CNT due to the lower surface roughness of PVA-Ni-D coating that can effectively seal cracks, crevices, and pores, leading to strong interfacial interlocking between reinforcements and matrix. The improved wear resistance of composite coatings was further allied with theoretical tribological parameters (contact depth, contact radius and shear

stress) and interfacial interaction calculations. The composite coating's geometrical, bonding, and electrical feature calculations, which revealed the highest binding energy, further supported the diamonds' strong interlocking. Owing to its amended mechanical, tribological and bonding characteristics, PVA-Ni-D coating exhibits potential utility in several engineering applications.

Data availability

Data will be made available on genuine request.

Conflicts of interest

The authors declare no conflict of interest.

Acknowledgements

S. A. acknowledges the Department of Chemistry, Manipal University, Jaipur, and the Department of Science and Technology (DST) Rajasthan, India, for providing a research grant (13(186)/2024-25/2603). S. K. P. thanks Maulana Azad National Institute of Technology, Bhopal, for providing a seed grant for research (Dean(R&C)/2024/2931).

References

1 N. Jain, V. K. Singh and S. Chauhan, A review on mechanical and water absorption properties of polyvinyl alcohol based composites/films, *J. Mech. Behav. Mater.*, 2017, **26**, 213–222, DOI: **10.1515/jmbm-2017-0027**.

2 H. F. Brinson and L. C. Brinson, *Polymer Engineering Science and Viscoelasticity*, Springer US, Boston, MA, 2008. DOI: **10.1007/978-0-387-73861-1**.

3 C. Verma, C. M. Hussain, M. A. Quraishi and K. Y. Rhee, Metals and metal oxides polymer frameworks as advanced anticorrosive materials: design, performance, and future direction, *Rev. Chem. Eng.*, 2024, **40**, 35–66, DOI: **10.1515/revce-2022-0039**.

4 T. M. Pollock, Alloy design for aircraft engines, *Nat. Mater.*, 2016, **15**, 809–815, DOI: **10.1038/nmat4709**.

5 D. Nunes, M. Vilarigues, J. B. Correia and P. A. Carvalho, Nickel-carbon nanocomposites: Synthesis, structural changes and strengthening mechanisms, *Acta Mater.*, 2012, **60**, 737–747.

6 Z. Ren, N. Meng, K. Shehzad, Y. Xu, S. Qu, B. Yu and J. K. Luo, Mechanical properties of nickel-graphene composites synthesized by electrochemical deposition, *Nanotechnology*, 2015, **26**, 65706–65714.

7 S. Awasthi, C. P. Pandey and K. Balani, Synergistic role of carbonaceous reinforcements on multi length scale tribology of electrophoretically deposited nickel-boron nitride coatings, *Mater. Res. Bull.*, 2018, **99**, 61–72.

8 S. Awasthi, S. K. Pandey, C. P. Pandey and K. Balani, Progress in Electrochemical and Electrophoretic Deposition of Nickel with Carbonaceous Allotropes, A Review, *Adv. Mater. Interfaces*, 2020, **7**, 1901096–1901129, DOI: **10.1002/admi.201901096**.

9 S. Awasthi and S. K. Pandey, Recent advances in smart hydrogels and carbonaceous nanoallotropes composites, *Appl. Mater. Today*, 2024, **36**, 102058, DOI: **10.1016/j.apmt.2024.102058**.

10 D. Zhang, C. Zhang, J. Liu, Q. Chen, X. Zhu and C. Liang, Carbon-Encapsulated Metal/Metal Carbide/Metal Oxide Core–Shell Nanostructures Generated by Laser Ablation of Metals in Organic Solvents, *ACS Appl. Nano Mater.*, 2019, **2**, 28–39.

11 B. Li, S. Xue, P. Mu and J. Li, Robust Self-Healing Graphene Oxide-Based Superhydrophobic Coatings for Efficient Corrosion Protection of Magnesium Alloys, *ACS Appl. Mater. Interfaces*, 2022, **14**, 30192–30204, DOI: **10.1021/acsami.2c06447**.

12 S. Xue, B. Li, P. Mu and J. Li, Designing attapulgite-based self-healing superhydrophobic coatings for efficient corrosion protection of magnesium alloys, *Prog. Org. Coat.*, 2022, **170**, 106966, DOI: **10.1016/j.porgcoat.2022.106966**.

13 A. K. Sonker, H. D. Wagner, R. Bajpai, R. Tenne and X. Sui, Effects of tungsten disulphide nanotubes and glutaric acid on the thermal and mechanical properties of polyvinyl alcohol, *Compos. Sci. Technol.*, 2016, **127**, 47–53, DOI: **10.1016/j.compscitech.2016.02.030**.

14 P. Verma, S. Anoop, V. Sasidhara Rao, A. K. Sharma and R. Uma Rani, Multiwalled carbon nanotube-poly vinyl alcohol nanocomposite multifunctional coatings on aerospace alloys, *Mater. Today Proc.*, 2018, **5**, 21205–21216, DOI: **10.1016/j.matpr.2018.06.520**.

15 J. Sun, Z. Fan, Y. Yang, C. Li, N. Tu, J. Chen and H. Lu, Tribological properties of aluminum alloy coated with graphene oxide/polyvinyl alcohol composites after micro-arc oxidation, *Ind. Lubr. Tribol.*, 2024, **76**, 500–512, DOI: **10.1108/ILT-12-2023-0427**.

16 N. Barhoumi, K. Khlifi, A. Maazouz and K. Lamnawar, Fluorinated Ethylene Propylene Coatings Deposited by a Spray Process: Mechanical Properties, Scratch and Wear Behavior, *Polymers*, 2022, **14**, 347, DOI: **10.3390/polym14020347**.

17 D. Rahmadiawan, H. Abral, S.-C. Shi, T.-T. Huang, R. Zainul, A. Ambiyar and H. Nurdin, Tribological Properties of Polyvinyl Alcohol/Uncaria Gambir Extract Composite as Potential Green Protective Film, *Tribol. Ind.*, 2023, **45**, 367–274, DOI: **10.24874/ti.1482.05.23.06**.

18 J. Joseph, A. Sharma, B. Sahoo, J. Paul and A. M. Sidpara, PVA/MLG/MWCNT hybrid composites for X band EMI shielding – Study of mechanical, electrical, thermal and tribological properties, *Mater. Today Commun.*, 2020, **23**, 100941, DOI: **10.1016/j.mtcomm.2020.100941**.

19 D. Ravnikar, R. S. Rajamure, U. Trdan, N. B. Dahotre and J. Grum, Electrochemical and DFT studies of laser-alloyed TiB2/TiC/Al coatings on aluminium alloy, *Corros. Sci.*, 2018, **136**, 18–27, DOI: **10.1016/j.corsci.2018.02.028**.

20 Y. Ge, J. Cheng, J. Mo, L. Xue, B. Zhang, S. Hong, Y. Wu, X. Liang and X. Zhang, Experimental and DFT studies on corrosion behaviors of laser-cladded (FeCoNi) 75−xCrxB15Si10 high-entropy alloy coatings, *J. Alloys Compd.*, 2024, **976**, 173173, DOI: **10.1016/j.jallcom.2023.173173**.

21 X. Ji, A. Seif, J. Duan, A. Rashidi, Z. Zhou, S. Pourhashem, M. Mirzaee, X. Zhai, X. Zhao and B. Hou, Experimental and DFT studies on corrosion protection performance of epoxy/graphene quantum dots@TiO2 nanotubes coatings, *Constr. Build. Mater.*, 2022, **322**, 126501, DOI: **10.1016/j.conbuildmat.2022.126501**.

22 R. M. A. Khalil, M. I. Hussain, N. Luqman, F. Hussain, A. M. Rana, M. S. Akhtar and R. F. Mehmood, DFT-based study of the structural, optoelectronic, mechanical and magnetic properties of Ti_3AC_2 (A = P, As, Cd) for coating applications, *RSC Adv.*, 2022, **12**, 4395–4407, DOI: **10.1039/D1RA07856A**.

23 S. Loftager, J. M. García-Lastra and T. Vegge, A density functional theory study of the carbon-coating effects on lithium iron borate battery electrodes, *Phys. Chem. Chem. Phys.*, 2017, **19**, 2087–2094, DOI: **10.1039/C6CP06312H**.

24 S. Awasthi, R. Maurya, C. P. Pandey and K. Balani, Interfacial mechanics of carbonaceous reinforcements in electrophoretically deposited nickel coatings, *Surf. Coat. Technol.*, 2017, **310**, 79–86, DOI: **10.1016/j.surfcoat.2016.12.039**.

25 N. P. Wasekar, P. Haridoss, S. K. Seshadri and G. Sundararajan, Influence of mode of electrodeposition, current density and saccharin on the microstructure and hardness of electrodeposited nanocrystalline nickel coatings, *Surf. Coat. Technol.*, 2016, **291**, 130–140, DOI: **10.1016/j.surfcoat.2016.02.024**.

26 N. A. Kozyrev, R. E. Kryukov and O. A. Kozyreva, New Tendencies in Development of Carbonaceous Additives for Welding Fluxes, *IOP Conf. Ser.: Mater. Sci. Eng.*, 2015, **91**, 012008, DOI: **10.1088/1757-899X/91/1/012008**.

27 S. Awasthi, B. Prior Palomero, A. Srivastava, S. Selvaraj and S. K. Pandey, Nanodiamond-structured zinc composite coatings with strong bonding and high load-bearing capacity, *Nanoscale Adv.*, 2024, **6**, 1001–1010, DOI: **10.1039/D3NA00809F**.

28 M. Chozhanathmisra, L. Murugesan, A. Murugesan, G. Palanisamy and R. Rajavel, Enhancement on physical, chemical, and biological properties of HNT-PVA-ALG-HAp biocomposite coating on implant substrate for biomedical application, *Ceram. Int.*, 2022, **48**, 16868–16876, DOI: **10.1016/j.ceramint.2022.02.241**.

29 S. Mezlini, P. Kapsa, J. C. Abry, C. Henon and J. Guillemenet, Effect of indenter geometry and relationship between abrasive wear and hardness in early stage of repetitive sliding, *Wear*, 2006, **260**, 412–421, DOI: **10.1016/j.wear.2005.02.106**.

30 N. Krishnamurthy, M. S. Prashantharedy, H. P. Raju and H. S. Manohar, A Study of Parameters Affecting Wear Resistance of Alumina and Yttria Stabilized Zirconia Composite Coatings on Al-6061 Substrate, *ISRN Ceram.*, 2012, **2012**, 1–13, DOI: **10.5402/2012/585892**.

31 S. Awasthi, S. K. Pandey and K. Balani, Tuning the magnetism and tribological behaviour of electrodeposited Ni/Cu bi-layer by selective reinforcement of carbon nanotubes, *J. Alloys Compd.*, 2020, **818**, 153287–153299, DOI: **10.1016/j.jallcom.2019.153287**.

32 M. J. Frisch, G. W. Trucks, H. B. Schlegel, G. E. Scuseria, M. A. Robb, J. R. Cheeseman, G. Scalmani, V. Barone, B. Mennucci, G. A. Petersson, H. Nakatsuji, M. Caricato, X. Li, H. P. Hratchian, A. F. Izmaylov, J. Bloino, G. Zheng, J. L. Sonnenberg and M. Had, *Gaussian* 09, Gaussian, Inc., Wallingford CT, 2009.

33 K. S. Hajeeassa, M. A. Hussein, Y. Anwar, N. Y. Tashkandi and Z. M. Al-amshany, Nanocomposites containing polyvinyl alcohol and reinforced carbon-based nanofiller, *Nanobiomedicine*, 2018, **5**, 184954351879481, DOI: **10.1177/1849543518794818**.

34 J. C. Ge, G. Wu, S. K. Yoon, M. S. Kim and N. J. Choi, Study on the Preparation and Lipophilic Properties of Polyvinyl Alcohol (PVA) Nanofiber Membranes via Green Electrospinning, *Nanomaterials*, 2021, **11**, 2514, DOI: **10.3390/nano11102514**.

35 M. Baghi, B. Niroumand, R. Emadi and M. Monirvaghefi, PVA Assisted Electroless Ni–P Coating of Carbon Fibers, *Trans. Indian Inst. Met.*, 2016, **69**, 1775–1781, DOI: **10.1007/s12666-016-0837-4**.

36 M. Chozhanathmisra, L. Murugesan, A. Murugesan, G. Palanisamy and R. Rajavel, Enhancement on physical, chemical, and biological properties of HNT-PVA-ALG-HAp biocomposite coating on implant substrate for biomedical application, *Ceram. Int.*, 2022, **48**, 16868–16876, DOI: **10.1016/j.ceramint.2022.02.241**.

37 K.-C. Zhou, H.-L. Pei, J.-K. Xiao and L. Zhang, Micro-scratch behavior of WC particle-reinforced copper matrix composites, *Rare Met.*, 2022, **41**, 2337–2342, DOI: **10.1007/s12598-015-0586-2**.

38 S. Awasthi, J. K. Gaur and M. S. Bobji, Advanced Ferrogels with High Magnetic Response and Wear Resistance Using Carbon Nanotubes, *J. Alloys Compd.*, 2020, **848**, 156259–156269.

39 S. Awasthi, S. Goel, C. P. Pandey and K. Balani, Multi-Length Scale Tribology of Electrophoretically Deposited Nickel-Diamond Coatings, *JOM*, 2017, **69**, 227–235, DOI: **10.1007/s11837-016-2142-4**.

40 M. M. Hasan, A. S. M. A. Haseeb and H. H. Masjuki, Structural and mechanical properties of nanostructured tungsten oxide thin films, *Surf. Eng.*, 2012, **28**, 778–785, DOI: **10.1179/1743294412Y.0000000066**.

41 C.-L. Kim, O. V. Penkov, D.-G. Shin and D.-E. Kim, Investigation of micro-abrasion characteristics of thin metallic coatings by *in situ* SEM scratch test, *Int. J. Precis. Eng. Manuf.*, 2016, **17**, 1139–1147, DOI: **10.1007/s12541-016-0138-1**.

42 M. Anand, G. Burmistroviene, I. Tudela, R. Verbickas, G. Lowman and Y. Zhang, Tribological evaluation of soft

metallic multilayer coatings for wear applications based on a multiple pass scratch test method, *Wear*, 2017, **388–389**, 39–46, DOI: **10.1016/j.wear.2017.01.119**.

43 B. D. Beake and T. W. Liskiewicz, Comparison of nano-fretting and nano-scratch tests on biomedical materials, *Tribol. Int.*, 2013, **63**, 123–131, DOI: **10.1016/j.triboint.2012.08.007**.

44 S. Venkatachalam and S. Y. Liang, Effects of Ploughing Forces and Friction Coefficient in Microscale Machining, *J. Manuf. Sci. Eng.*, 2007, **129**, 274–280, DOI: **10.1115/1.2673449**.

45 J.-K. Xiao, L. Zhang, K.-C. Zhou and X.-P. Wang, Microscratch behavior of copper–graphite composites, *Tribol. Int.*, 2013, **57**, 38–45, DOI: **10.1016/j.triboint.2012.07.004**.

46 P. Benjamin and C. Weaver, Measurement of adhesion of thin films, *Proc. R. Soc. London, Ser. A*, 1959, **254**, 163–176.

47 Z. Liu, Z. Yang, X. Wang, J. Liang, Z. Yang, H. Wu and G. Sha, Enhanced strength-ductility synergy in a new 2.2 GPa grade ultra-high strength stainless steel with balanced fracture toughness: Elucidating the role of duplex aging treatment, *J. Alloys Compd.*, 2022, **928**, 167135, DOI: **10.1016/j.jallcom.2022.167135**.

48 M. M. Gudarzi and F. Sharif, Enhancement of dispersion and bonding of graphene-polymer through wet transfer of functionalized graphene oxide, *eXPRESS Polym. Lett.*, 2012, **6**, 1017–1031, DOI: **10.3144/expresspolymlett.2012.107**.

49 A. K. Srivastava, S. K. Pandey and N. Misra, ($CH_3Br\cdots NH3$)@C60: The effect of nanoconfinement on halogen bonding, *Chem. Phys. Lett.*, 2016, **662**, 240–243, DOI: **10.1016/j.cplett.2016.09.036**.

50 S. K. Pandey, S. Hossain and E. Arunan, New Insights into the Formation of CH_3OCH_3 and CH_3SCH_3 without and with the Assistance of Na^+ Ions and Some Implications for Interstellar Chemistry: An *In Silico* Approach, *ACS Earth Space Chem.*, 2023, **7**, 388–403, DOI: **10.1021/acsearthspacechem.2c00292**.

51 A. A. Mini, A. Chakravorty, S. Das, S. Awasthi, A. N. Grace, S. K. Pandey and V. Raghavan, CuO nanoparticles passivated 2D MXene-based voltammetric sensor for detecting environmental hazardous pollutant, *Microchem. J.*, 2024, **201**, 110648, DOI: **10.1016/j.microc.2024.110648**.

52 X. Zong, H. Dahiya, Y. Song, X. Liang, S. K. Pandey, H. Xu and G. D. Sharma, Alkynyl BODIPY-Core Bridged Perylene Diimide Star-Shaped Nonfullerene Acceptors for Efficient Polymer Solar Cells, *ACS Appl. Energy Mater.*, 2022, **5**, 15624–15637, DOI: **10.1021/acsaem.2c03200**.

53 S. K. Pandey, Novel and Polynuclear K- and Na-Based Superalkali Hydroxides as Superbases Better Than Li-Related Species and Their Enhanced Properties: An Ab Initio Exploration, *ACS Omega*, 2021, **6**, 31077–31092, DOI: **10.1021/acsomega.1c04395**.

54 S. Awasthi, B. Prior Palomero, A. Srivastava, S. Selvaraj and S. K. Pandey, Nanodiamond-structured zinc composite coatings with strong bonding and high load-bearing capacity, *Nanoscale Adv.*, 2024, **6**, 1001–1010, DOI: **10.1039/D3NA00809F**.